HEALTH AND MEDICINE

Tough and tunable scaffold-hydrogel composite biomaterial for soft-to-hard musculoskeletal tissue interfaces

Raul A. Sun Han Chang[1], John F. Shanley[2], Mariana E. Kersh[2], Brendan A.C. Harley[1,3]*

Tendon inserts into bone via a fibrocartilaginous interface (enthesis) that reduces mechanical strain and tissue failure. Despite this toughening mechanism, tears occur because of acute (overload) or degradative (aging) processes. Surgically fixating torn tendon into bone results in the formation of a scar tissue interface with inferior biomechanical properties. Progress toward enthesis regeneration requires biomaterial approaches to protect cells from high levels of interfacial strain. We report an innovative tissue reinforcement strategy: a stratified scaffold containing osseous and tendinous tissue compartments attached through a continuous polyethylene glycol (PEG) hydrogel interface. Tuning the gelation kinetics of the hydrogel modulates integration with the flanking compartments and yields biomechanical performance advantages. Notably, the hydrogel interface reduces formation of strain concentrations between tissue compartments in conventional stratified biomaterials that can have deleterious biological effects. This design of mechanically robust stratified composite biomaterials may be appropriate for a broad range of tendon and ligament-to-bone insertions.

INTRODUCTION

The enthesis is a stratified fibrocartilaginous tissue (250 to 500 μm wide) that contains gradients in cell phenotype, biochemical cues, mineral content, matrix composition, and structural alignment to provide a transition zone through which tendon attaches into bone (1). This unique interfacial tissue microenvironment facilitates functional load bearing by providing a continuous energy-absorbing zone of high compliance, an important tissue toughening mechanism under tensile loads (2, 3). The classic enthesis injury is the rotator cuff tear, where acute overload, degeneration with age, or a combination of the two leads to partial or full-width tears within the tendon-to-bone enthesis. Surgical reattachment of tendon to bone is the clinical standard but leads to formation of narrow fibrovascular scar tissue rather than a graded fibrocartilage enthesis. The resultant sharp boundary between mechanically mismatched tendon and bone leads to strain concentrations that substantially increase the risk of refailure (>90% in some older demographics) (4). Functional reintegration of the torn tissues requires regeneration of the compliant fibrocartilaginous interface; however, progress toward regenerative strategies for enthesis repair is hampered by a lack of biomaterial designs able to meet the unique functional requirements of these tissues.

Stratified biomaterials offer potential advantages for enthesis repair. These biomaterials may selectively present optimized patterns of signals with features such as composition, structure, and mechanics tailored within discrete regions to spatially regulate cell bioactivity and tissue remodeling. This stratified, spatially controlled biological response is essential to recapitulate the distinct tissue microenvironments across the enthesis. To this end, we recently described a lyophilization method to fabricate a biphasic collagen scaffold containing both tendinous (anisotropic) and osseous (mineralized) compartments with distinct composition and microstructure con-

nected by a continuous interface (5). The mineralized osseous compartment promotes mesenchymal stem cell (MSC) osteogenic differentiation and improves bone regeneration without supplemental osteogenic factors. The nonmineralized anisotropic tendinous compartment promotes transcriptomic stability of primary tenocytes and induces MSC tenogenic differentiation (5–13). However, this biphasic scaffold and most biomaterials for tendon-to-bone enthesis repair to date replicate the enthesis as a gradient transition between tendon and bone rather than a unique multiscale tissue. While notable progress has been made in biomaterials for tendon and bone repair, the inherent mechanical mismatch between tissue analogous compartments in biomaterials can be biologically and mechanically detrimental for enthesis repair (14–17). Muscle loading is required for the development and maintenance of tendon, bone, and the enthesis and is unavoidable following injury and repair (1, 18–20). In this study, we show that cadaveric human shoulders have the potential for substantial strain concentrations at the tendon-to-bone insertion when subjected to torque-driven tensile loading, a trait that is dependent upon the bulk stiffness of the shoulder. In loaded stratified enthesis biomaterials, mechanical mismatch at the interface between dissimilar tendinous and osseous regions similarly results in strain concentrations that can considerably reduce cell viability and become a likely point of fracture. Hence, the resulting interfacial strain leads to a dampened cellular response and graft failure at the precise location where regeneration is needed.

Here, we report development and validation of a unique biomaterial reinforcement motif inspired by structure-function properties of the native enthesis: inclusion of a compliant hydrogel interface between mechanically mismatched tendinous and osseous tissue compartments (2, 3, 21). While common in engineering materials, these design elements have not been previously explored in tissue engineering biomaterials. We have developed an approach to control the insertion and stabilization of a compliant polyethylene glycol (PEG) hydrogel zone between the tendinous and osseous compartments of our previously described biphasic collagen scaffold. The resulting triphasic biomaterial is different from layered two-phase or three-phase biomaterials that lack a continuous interface.

[1]Department of Chemical and Biomolecular Engineering, University of Illinois at Urbana-Champaign, Urbana, IL 61801, USA. [2]Department of Mechanical Science and Engineering, University of Illinois at Urbana-Champaign, Urbana, IL 61801, USA. [3]Carl R. Woese Institute for Genomic Biology, University of Illinois at Urbana-Champaign, Urbana, IL 61801, USA.
*Corresponding author. Email: bharley@illinois.edu

We show that tuning the fabrication parameters of this hydrogel zone provides a robust method to reduce levels of strain concentrations that form at a mismatched bimaterial interface. Inclusion of a hydrogel enthesis also markedly improves the macroscale mechanical performance of the entire tissue scaffold and provides a new design paradigm for tissue engineering approaches to improve healing for a wide range of musculoskeletal tissue insertions.

RESULTS

A hydrogel stably integrates dissimilar tissue scaffold compartments

We used a horseradish peroxidase (HRP)–mediated chemical polymerization to covalently cross-link four-arm PEG-thiol (PEG-SH) monomers into an interfacial hydrogel network (Fig. 1A) (22). This class of reaction introduces tunability in cross-linking rate and hydrogel material properties (e.g., elasticity), both of which can be quantified via small-amplitude oscillatory shear (SAOS) rheometry through conventional (t_{cross} and G'_{eq}) and previously unidentified (Δt_{gel}) parameters of gelation (fig. S1) (23, 24). Here, t_{cross} defines the time it takes to transition from a predominantly viscous ($G' < G''$) to an elastic ($G' > G''$) material, while the equilibrium storage modulus (G'_{eq}) is a measure of a material's elastic response. Recently, we reported the use of Δt_{gel}, derived from the time derivative of G', to quantify the duration over which considerable changes in viscoelastic properties occur, from the onset of measurable gelation to reaching an equilibrium gel state (24). We selected a test set of PEG-SH hydrogels spanning gelation properties to match the time scale for lyophilization-based scaffold fabrication (t: 0 to 60 min) (25, 26) with a range of elastic behavior (G'_{eq}: 4 to 15 kPa) from a library of previously characterized hydrogels (Table 1) (24).

To fabricate continuous triphasic scaffolds, we adapted a copper–polytetrafluoroethylene (PFTE) mold (fig. S2) that allows horizontal loading of liquid suspensions for precise layers and controlled phase interdiffusion before lyophilization (Fig. 1B). After lyophilization, structurally continuous triphasic scaffolds are formed with a PEG hydrogel interfacial layer connecting the tendinous and osseous scaffold compartments (Fig. 1C). The thermal conductivity mismatch between copper and PFTE at one end of the mold establishes localized directional solidification to induce formation of an anisotropic, nonmineralized (tendinous) scaffold compartment, while at the opposing end, an isotropic mineralized (osseous) collagen scaffold structure is formed (fig. S3).

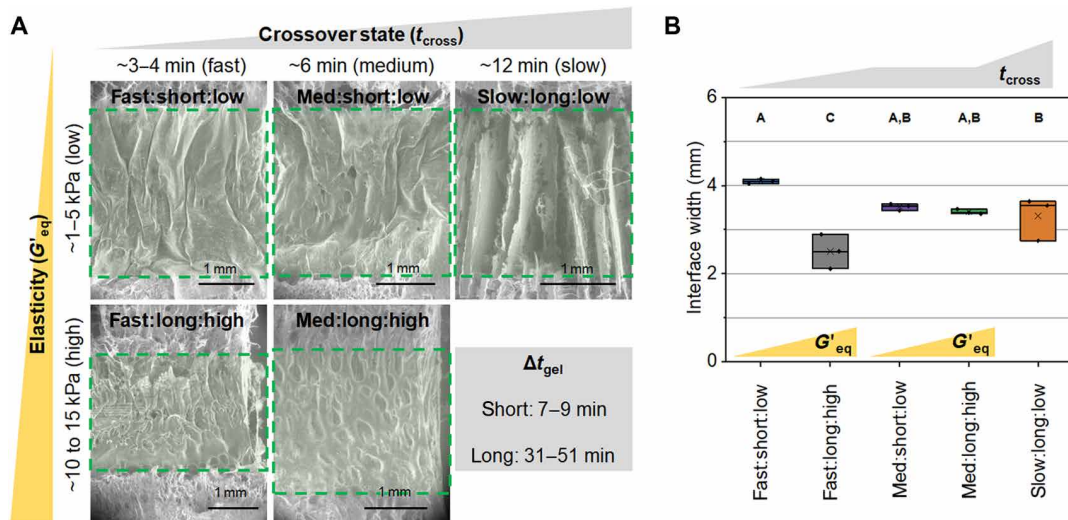### Integration and topology of interfacial hydrogels depends on gelation kinetics

Environmental scanning electron microscopy (ESEM) images of triphasic scaffolds demonstrate that the topology and extent of incorporation of the interfacial hydrogel seam can be adapted by varying the hydrogel gelation properties. Overall, faster gelling hydrogels (fast t_{cross} and short Δt_{gel}) are more uniformly incorporated into scaffolds in distinct, monolithic hydrogel layers, whereas the slowest gelling hydrogel is distributed within the collagen fibers of the flanking tissue compartments (Fig. 2A), likely due to extended diffusive mixing between the hydrogel and collagen suspensions. The width of the scaffold-hydrogel interface is also controlled via gelation (Fig. 2B), allowing fabrication of triphasic scaffolds with unique interfacial zones based on a range of hydrogel gelation properties. Hydrogel interfaces were classified as having fast (3 to 4 min), medium (6 min), or slow (12 min) t_{cross}; short (7 to 9 min) or long (31 to 51 min) Δt_{gel}; and low (1 to 5 kPa) or high (10 to 15 kPa) G'_{eq} (e.g., fast t_{cross}, short Δt_{gel}, and low G'_{eq} is fast:short:low). We report fabrication and mechanical performance of a series of triphasic scaffolds based on a range of hydrogel gelation properties. Here, triphasic scaffolds are identified via these unique gelation parameters (t_{cross}:Δt_{gel}:G'_{eq}) that describe time to viscous-elastic transition (t_{cross}), time to complete gelation (Δt_{gel}), and final elastic properties (G'_{eq}) of the hydrogel interface.
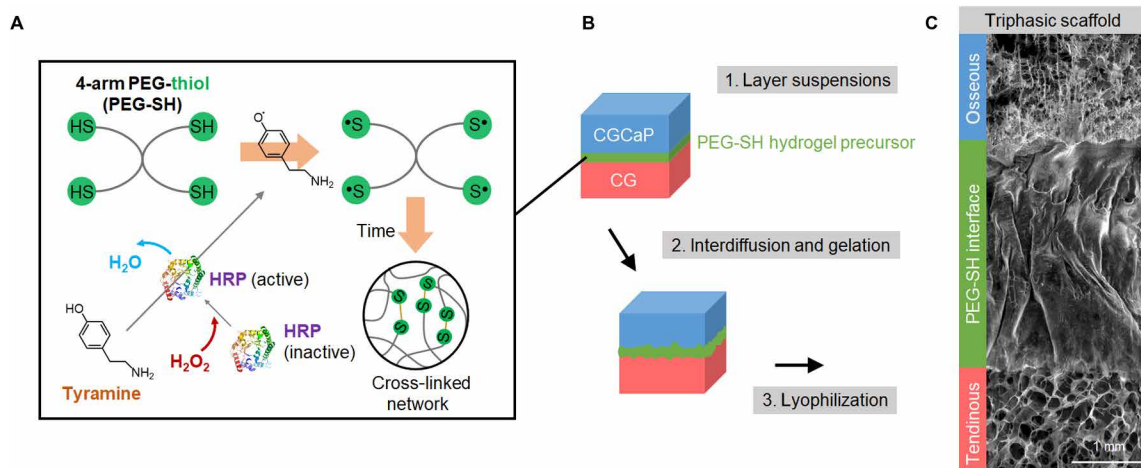
Fig. 1. PEG hydrogel cross-linking reaction and triphasic scaffold fabrication. (**A**) Formation of a cross-linked PEG network via HRP catalyzed cross-linking. Initially, hydrogen peroxide (H_2O_2) reacts with HRP in its inactive state. Activated HRP oxidizes tyramine to form phenolic radicals that will oxidize thiol groups. Thiol groups on 4-arm PEG-thiol (PEG-SH) monomers are oxidized to thiol radicals that readily form disulfides over time to create a cross-linked polymer network. (**B**) A suspension-layering lyophilization method is used to incorporate a PEG hydrogel layer between tendinous (CG) and osseous (CGCaP) collagen-GAG compartments. First, CG and CGCaP liquid suspensions and the PEG hydrogel precursor solution are layered into a mold and allowed to mix diffusively at their interface as the PEG precursor solution gels. (**C**) Following lyophilization, structurally continuous triphasic scaffolds are generated with a distinct interfacial PEG hydrogel layer between tendinous and osseous tissue compartments.

Table 1. A test set of hydrogel samples [varying PEG-SH (wt %) and H$_2$O$_2$ (mM) with tyramine (5 mM) and HRP (5 U/ml) held constant] with a range of t_{cross}, Δt_{gel}, and G'_{eq} was identified from previously reported SAOS measurements (24). The following naming convention was used to distinguish samples based on their gelling characteristics: time to reach crossover state (fast, medium, or slow), duration of gelation interval (short or long), and magnitude of G'_{eq} (low or high). Reported values of t_{cross}, Δt_{gel}, and G'_{eq} are average ± SD ($n = 3$).

Sample	PEG-SH (wt %)	H$_2$O$_2$ (mM)	t_{cross} (min)	Δt_{gel} (min)	G'_{eq} (kPa)	t_{cross}:Δt_{gel}:G'_{eq}
P5H5	5	5	5.8 ± 0.6	6.8 ± 1.1	4.0 ± 0.5	Med:short:low
P5H10	5	10	3.0 ± 0.4	8.8 ± 2.2	5.0 ± 0.2	Fast:short:low
P10H5	10	5	11.9 ± 2.7	51.2 ± 12.9	1.0 ± 0.4	Slow:long:low
P10H8	10	8	5.8 ± 0.4	31.4 ± 1.9	10.8 ± 0.3	Med:long:high
P10H10	10	10	4.6 ± 0.2	32.9 ± 4.5	15.8 ± 0.4	Fast:long:high

Fig. 2. Interfacial hydrogel topology and width. (**A**) Representative ESEM images of triphasic scaffolds show that incorporation of the interfacial hydrogel phase (green dashed line region) and (**B**) interface width are dependent on the hydrogel gelation. Groups not sharing a letter are significantly different ($P < 0.05$). Triphasic scaffolds are identified via unique interface hydrogel gelation parameters (t_{cross}:Δt_{gel}:G'_{eq}) that describe time to viscous-elastic transition (t_{cross}), time to complete gelation (Δt_{gel}), and final elastic properties (G'_{eq}).

## Interfacial hydrogels modulate bulk scaffold response to tensile loading

We demonstrated that gelation-dependent incorporation of a compliant hydrogel seam is an effective toughening mechanism in scaffolds under uniaxial tension (fig. S4). Bulk scaffold toughness was significantly increased in triphasic scaffolds containing fast gelling (t_{cross}) hydrogel formulations (fast:long:high and fast:slow:low) compared to biphasic scaffolds that lack a hydrogel insertion (Fig. 3A). Toughness appeared not to be strongly influenced by overall gelation time (Δt_{gel}) or elastic properties (G'_{eq}) of the hydrogel phase. Fast gelling enthesis variants also display significantly higher toughness than other variants with slower t_{cross} (e.g., med:long:high), indicating that within our fabrication scheme, a particular time scale of gelation is required to incorporate a toughening interfacial hydrogel.

The mechanism by which fast t_{cross} hydrogels increase toughness differs (Fig. 3B). Hydrogels with long Δt_{gel} and high G'_{eq} (fast:long:high) significantly increase ultimate tensile strength (Fig. 3C) and elastic modulus (Fig. 3E) of triphasic scaffolds, resulting in a steeper stress-strain curve and increased maximal stress withstood. Comparatively, hydrogels with short Δt_{gel} and low G'_{eq} (fast:short:low) significantly increase strain tolerated before fracture

(Fig. 3D) and display a significantly lower elastic modulus, resulting in more ductile triphasic scaffolds. These distinct toughening mechanisms are apparent under applied physiological strains (Fig. 3, F and G). Up to a maximum applied strain of 3%, more ductile (higher strain at fracture) fast:short:low variants display significantly lower toughness than higher stiffness fast:long:high variants due to comparatively lower levels of stress.

Hydrogels dissipate interfacial strain between mechanically disparate tissue compartments

We used digital image correlation (DIC) to map local strain on full-length scaffolds to determine whether toughening interfacial hydrogels also influenced the distribution of strain in scaffolds under uniaxial tension (27, 28). Strain distributions are reported using an identical scale for all scaffolds to facilitate comparison between experimental groups (Fig. 4) and using individualized scales for more accurate visualizations of strain within experimental groups (fig. S5). At 3.3% bulk applied strain, biphasic scaffolds display a sharp strain (~10%) concentrated at the interface between tendinous and osseous tissue compartments, which is ultimately the point of fracture at 3.5% bulk applied strain (Fig. 4A and fig. S5A). Triphasic
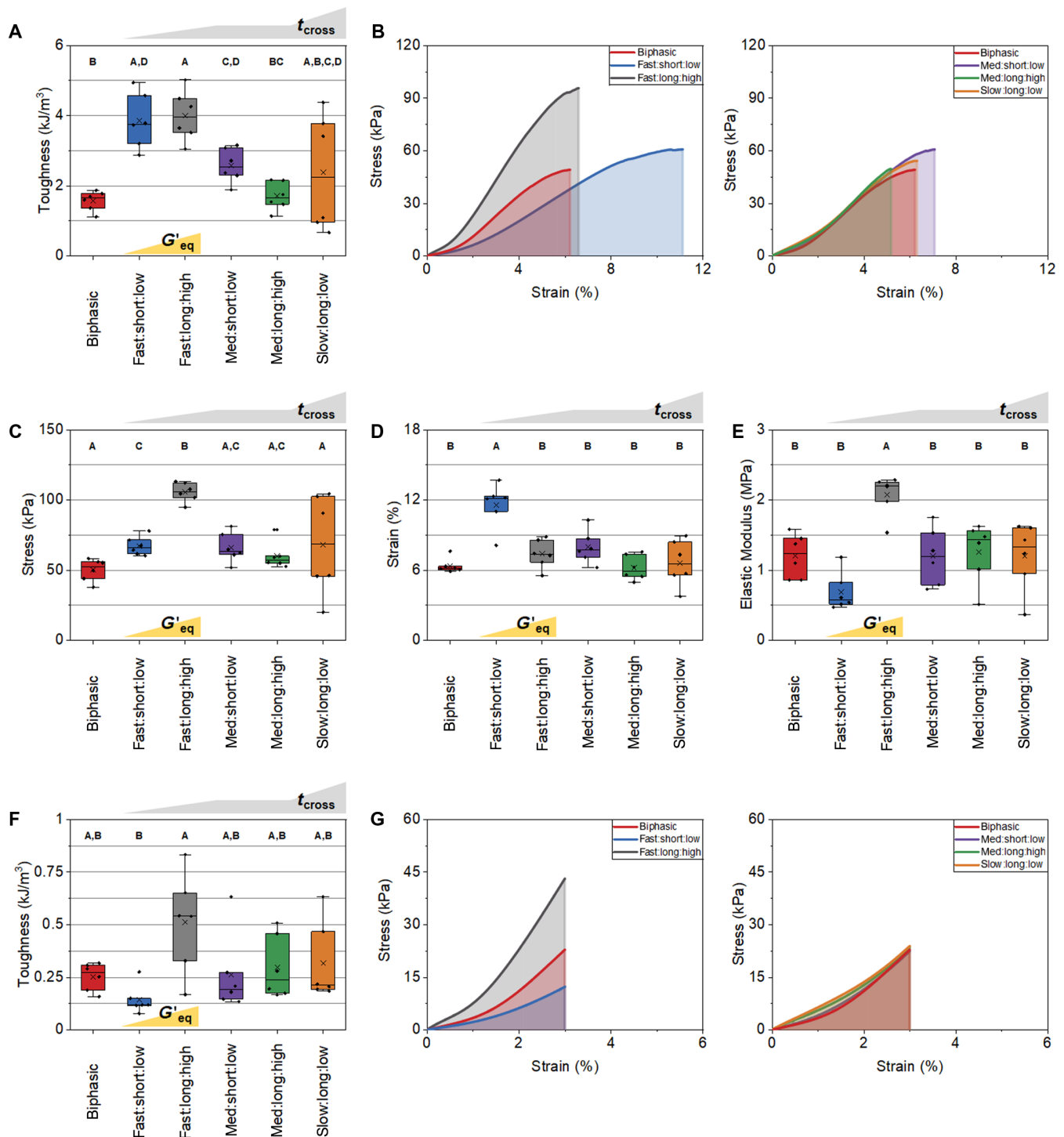
Fig. 3. Bulk scaffold mechanical properties under uniaxial tension. (**A**) Bulk scaffold toughness through the point of failure. (**B**) Averaged stress-strain curves for highest-toughness triphasic scaffold variants (left) and all other triphasic variants (right) versus biphasic scaffolds. (**C**) Maximum tensile stress and (**D**) strain at scaffold fracture. (**E**) Bulk elastic modulus of scaffolds. (**F**) Bulk scaffold toughness up to physiological levels of strain (3%). (**G**) Averaged stress-strain curves for highest-toughness triphasic scaffold variants (left) and all other triphasic variants (right) versus biphasic scaffolds up to physiological levels of strain (3%). Groups not sharing a letter are significantly different ($P < 0.05$). For stress-strain curves, linear interpolation was used to average multiple stress-strain curves for each scaffold. Triphasic scaffolds are identified via unique interface hydrogel gelation parameters (t_{cross}:Δt_{gel}:G'_{eq}) that describe time to viscous-elastic transition (t_{cross}), time to complete gelation (Δt_{gel}), and final elastic properties (G'_{eq}).
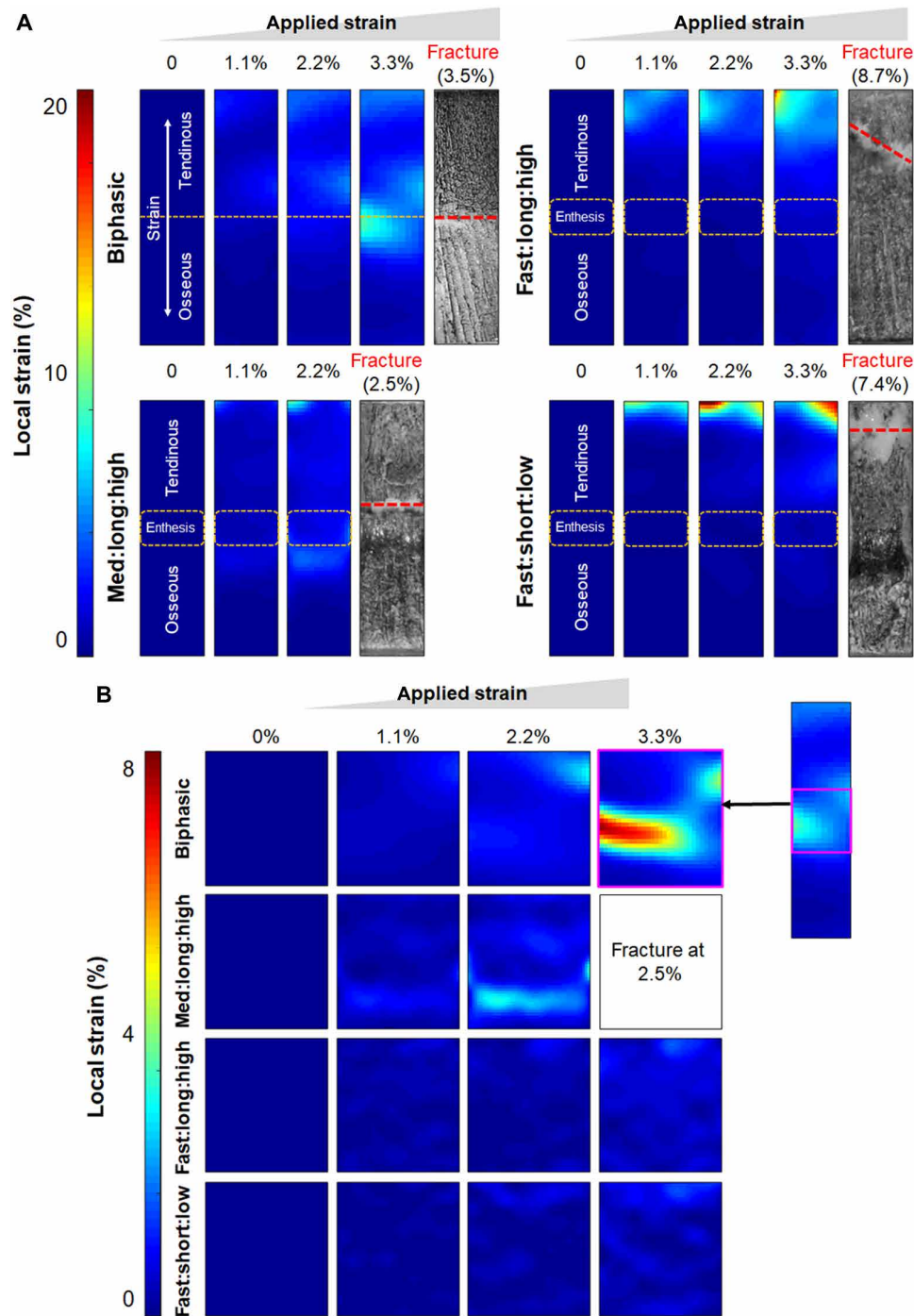
Fig. 4. Local strain profiles across scaffolds under uniaxial tension. (**A**) Representative profiles of local strain across the entire scaffold and (**B**) within the middle regions of biphasic, med:long:high, fast:long:high, and fast:slow:low scaffolds at global applied strains of 0, 1.1, 2.2, and 3.3% (strains are with respect to the full-length scaffolds). See fig. S5 for individually scaled heatmaps of local strain across scaffolds. Triphasic scaffolds are identified via unique interface hydrogel gelation parameters (t_{cross}:Δt_{gel}:G'_{eq}) that describe time to viscous-elastic transition (t_{cross}), time to complete gelation (Δt_{gel}), and final elastic properties (G'_{eq}).

variants that do not significantly increase toughness compared to biphasic scaffolds show similar strain concentrations at the biomaterial interface. For example, the med:long:high variant displays ~5% strain at the interface in response to 2.2% bulk applied strain, ultimately fracturing at the interface under 2.5% bulk applied strain.

However, the higher toughness triphasic variants display markedly reduced strain at the interface and heightened strain in the more elastic tendinous compartment, where they ultimately fracture at 8.7 and 7.4% bulk applied strain. We subsequently examined the strain profiles within only the transition zones between tendinous

and osseous tissue compartments to obtain a clearer representation of interfacial strain (Fig. 4B and fig. S5B). At 3.3% bulk applied strain, the biphasic scaffold interface develops sharp strain concentrations (7.2%) greater than the applied global strain, whereas higher toughness triphasic scaffolds show evenly distributed interfacial strains (~2%) that are less than the overall bulk applied strain. Furthermore, triphasic scaffolds exhibit lower interfacial strain variability in the transverse direction than biphasic scaffolds, indicating that interfacial hydrogels have more uniform strain along their width (fig. S6).

Human shoulders exhibit stiffness-dependent changes in local tissue strain

We examined strain distributions across the supraspinatus tendon and shoulder capsule from cadaveric human donors. The supraspinatus tendon was fixed onto a testing apparatus and a torque-load applied, resulting in tensile loading of the tendon-to-bone insertion at the local tissue level. This local tensile loading provided the opportunity to evaluate strain concentrations at the enthesis and surrounding tendon (fig. S1A). In a higher stiffness specimen (114.6 N/mm), tensile loading resulted in negligible strain concentrations near the enthesis (fig. S1B). However, in a lower stiffness specimen (15.1 N/mm), tensile loading resulted in ~14% strain concentrated at or near the enthesis.

DISCUSSION

Biomaterials that mimic the structural complexity and/or functional features of missing or injured tissues are an essential component of tissue engineering strategies to improve patient outcomes. Effective regenerative scaffolds may provide instructive cues to help guide cell behavior toward tissue-relevant processes (e.g., differentiation and matrix remodeling). Achieving these results is particularly challenging in the case of soft-to-hard musculoskeletal tissue interfaces. These specialized transitional zones transmit loads and minimize strain concentrations that would otherwise form at the junction between soft tissues (e.g., tendon, ligament, and cartilage) and bone. Musculoskeletal interfaces are especially susceptible to injury due to high strain that can form at the junction between two biomechanically disparate tissues under physiological loads (29). Conventional surgical solutions for tendon-to-bone insertion repair often fail at the bony insertion site due to insufficient tissue integration, underscoring the importance of an integrating interface in maintaining efficacy and function (30). To date, biomaterials developed for enthesis repair at best consider the enthesis as a third tissue compartment in a stratified material rather than a multiscale transitional tissue. Our findings suggest that the connectivity between soft and hard tissue compartments should be an essential biomaterial design criterion.

Bimaterial interfaces connecting dissimilar materials pose a substantial challenge due to the development of stress concentrations that can result in failure at the interface under mechanical loads smaller than what is required for failure to occur in either material alone (3, 31). To robustly incorporate dissimilar materials, strategies are required that dissipate instances of interfacial stress and resultant high deformation. Functionally graded materials containing a transition in material properties have been used to reduce stress concentrations, but a distinct transitional material that effectively dissipates stress has not been explored. An added layer of complexity arises within stratified multi-tissue scaffold structures that must integrate materials with not only differences in mechanics but also unique compositional and biochemical properties.

Stratified tissue scaffolds can be created by fusing individually processed materials into a single construct or by simultaneously processing and integrating different phases during fabrication (32–35). We previously developed a process to create biphasic scaffolds integrating osseous and tendinous phases via liquid layering, where diffusive mixing between mineralized and nonmineralized collagen suspensions followed by lyophilization creates a porous scaffold with distinct tissue compartments but a continuity of collagen fibers across a sharp interface. While this interface resists delamination while handling the scaffold, under tension, the interface is subject to high strain and eventual fracture, as is the case in similar scaffolds incorporating mechanically dissimilar phases (35). Here, we hypothesize that a similar layering and fusing approach could be used with a third, enthesis-specific interfacial PEG hydrogel. Given that the native enthesis incorporates a fibrocartilaginous interfacial tissue that is more compliant than flanking tendon and bone (3), we hypothesized that a hydrogel layer could serve a similar role within a tissue scaffold. PEG has been used for a wide range of tissue engineering applications due to its noncytotoxicity and the diverse functional groups that can be added to its backbone to facilitate cross-linking, degradability, improved bioactivity, and biomolecular functionalization, thereby providing a canvas for locally presenting cues to alter cellular response (36–39). Enzymatic cross-linking can generate strong covalent bonds between polymer chains under mild conditions amenable to encapsulation of drugs, proteins, and living cells. The reported hydrogel insertion uses HRP as an oxidation-catalyzing enzyme to generate a cross-linked PEG network via radical coupling of thiol groups in the presence of exogenous hydrogen peroxide (H_2O_2) (40). This HRP-catalyzed gelation can be accelerated by phenolic compounds such as tyramine (22) and hence can offer tunability regarding gelation rate and final gel properties (e.g., elasticity).

Previous work by our group has shown that gelation rate and elasticity of HRP-catalyzed PEG-SH hydrogels can be tuned via polymer weight percent and H_2O_2 concentration and precisely monitored via small-angle oscillatory shear rheometry (24). Here, we show that tuning the rate of hydrogel gelation influences the formation and subsequent mechanical performance of a continuous hydrogel interface between dissimilar scaffold compartments. A central feature of our fabrication scheme is identifying time scales of hydrogel gelation that permit formation of a stable hydrogel interface. These time scales balance considerations of hydrogel gelation versus diffusive mixing of the hydrogel precursor and flanking collagen suspensions before freeze-drying. We reasoned that two time-dependent gelation processes may directly affect this process: (i) the point at which the hydrogel transitions into an elastically behaving solid (t_{cross}) and (ii) the point at which the elastic properties of the hydrogel are no longer changing with time (Δt_{gel}). Physically, t_{cross} indicates the time scale at which a sol-gel transition occurs; however, information regarding the entire duration over which gelation occurs is not represented by t_{cross}. Comparatively, Δt_{gel} defines the duration over which the derivative of G' is nonzero and indicates the interval over which considerable changes in viscoelasticity occur. Together, these properties represent the overall rate of gelation and dictate the hydrogel response to diffusive mixing over time. In addition to examining the role of time-dependent gelation properties on functional performance of the resultant

triphasic biomaterial, we also hypothesized that the energy-storing properties of the hydrogel interface (G'_{eq}) would play a direct role in mechanical performance, notably the ability to reduce interfacial strain concentrations and improve toughness under tensile stimulation.

Tuning gelation properties of the incorporated hydrogel phase directly modulates resultant interfacial integration and mechanical properties. Hydrogels that quickly become viscous (t_{cross}: 3 to 4 min), regardless of time required to fully gel (Δt_{gel}), optimally integrate between flanking collagen suspensions during liquid-phase layering and form mechanically robust triphasic scaffolds. Furthermore, differences in hydrogel storage modulus between the higher toughness variants (fast:long:high and fast:short:low) did not directly influence the magnitude of toughness, indicating that within the range of tested G'_{eq} (5 to 15 kPa), matching the hydrogel gelation with diffusive incorporation and lyophilization time scales is the key determinant of scaffold toughness. However, the elastic properties of the hydrogel phase control the mechanism by which toughening of the bulk scaffold occurs. Therefore, stable hydrogel incorporation seems to be largely dependent upon the time scale of t_{cross} and is defined by the formation of a distinct and monolithic hydrogel phase. Once properly integrated, the storage modulus of the hydrogel dictates the energy-absorbing properties at the interface, which, in turn, modulate the mechanical behavior of the entire construct. A material that stores more energy (higher G'_{eq}) at the interface increases the bulk stress withstood up to failure, whereas a less energy-absorbing material (lower G'_{eq}) increases the bulk strain withstood up to failure.

The inclusion of a hydrogel enthesis also notably alters the mode of failure and the local strain experienced by scaffolds under tensile loading. Grossly, biphasic scaffolds that lack a hydrogel enthesis fail at the tendinous-osseous interface due to large concentrations of strain, whereas triphasic variants displaying increased toughness fracture in one of the collagen compartments and away from the scaffold interface, where strain has been effectively dissipated. Comparatively, triphasic variants that did not exhibit increases in bulk toughness also fail at the interface, given that these hydrogels have not been stably integrated into the scaffold. Tuning hydrogel gelation properties to optimize integration of a compliant interfacial zone provides a facile way to improve overall mechanical performance and reduce localized strain concentrations between mechanically dissimilar biomaterial compartments. We foresee that the design paradigm reported here, namely, inclusion of a continuous, compliant hydrogel interface that markedly reduces strain concentrations between mechanically dissimilar biomaterials, may be broadly applicable for stratified biomaterials being developed as regenerative medicine templates for a range of musculoskeletal tissues such as the tendon-bone, ligament-bone, or muscle-tendon insertions.

Tensile strain in our scaffolds was compared to tensile strain in cadaveric human shoulders undergoing simulated supraspinatus muscle loads. Following arthroscopic rotator cuff repair, patients who developed shoulder stiffness at 6 and 12 weeks postoperatively experienced better rotator cuff integrity at 6 months postoperatively (41). These outcomes show that postoperative stiffness is associated with improved healing of the tendon-to-bone insertion of the rotator cuff. In our study, the higher stiffness shoulder specimen did not exhibit strain concentrations at the tendon-to-bone insertion under tensile loads in a manner similar to that of our higher toughness triphasic scaffolds (fig. S7). However, the lower stiffness shoulder specimen exhibited strain concentrated near the insertion between tendon and bone similar to biphasic scaffolds.

Our evaluation of toughness and mechanical performance of hydrogel insertions does not take into consideration the existence of pre-existing flaws or tears. Fracture toughness describes a material's ability to resist crack propagation and, in the case of the native enthesis, involves microscale mechanisms such as fiber realignment and fiber densification (2, 3, 20, 42–45). While studies measuring fracture toughness of triphasic biomaterials will be critical in optimization of mechanical performance for in vivo applications, the goal of the present study is to describe a novel biomaterial design paradigm. We show that stable integration of a compliant hydrogel between disparate tissue regions improves mechanical performance by reducing the formation of local strain concentrations under tensile load. However, it will be imperative in future studies seeking to optimize biomechanical performance of the hydrogel insert to consider fracture mechanisms and microscale mechanical behavior at the scaffold-hydrogel interface, particularly the role of microscale mechanics on cell activity.

Ultimately, we demonstrate fabrication and validation of a previously unidentified class of tough, stratified biomaterials for repair of enthesis injuries. Inclusion of a compliant hydrogel interface between dissimilar collagen scaffolds provides a bioinspired reinforcement approach to effectively dissipate local strains between dissimilar biomaterial environments and reduce the prevalence of failure at the interface. We show that altering hydrogel gelation properties, notably the time required for viscous to elastic transition and the final elastic properties of the hydrogel network, provides a powerful tool to improve the mechanical performance of the resulting triphasic biomaterial. This model for tough composite biomaterials may offer insight regarding bioinspired toughening of stratified composite materials and design of robust tissue scaffolds for a range of orthopedic insertion injuries.

MATERIALS AND METHODS
Preparation of hydrogels and rheological analysis of gelation parameters
The subset of hydrogels incorporated into triphasic scaffolds was selected from a previously characterized library of hydrogels (24). Four-arm PEG-thiol (PEG-SH) hydrogel precursor solutions were generated from mixtures of 4-arm PEG-thiol [PEG-SH; 20,000 weight-average molecular weight (M_w); JenKem Technology, Plano, TX] dissolved in Dulbecco's phosphate-buffered saline (DPBS) (pH 7.3; Corning cellgro, Corning, New York) mixed with a reaction solution generated from H_2O_2 (30% solution, Macron, Radnor, PA), tyramine (99%, Sigma-Aldrich, St. Louis, MO), and HRP (Thermo Fisher Scientific, Waltham, MA). All samples contained a fixed amount of tyramine (5 mM) and HRP (5 U/ml). The polymer and reaction solutions were mixed to generate the polymerizing hydrogel solution. After mixing, samples were immediately loaded onto the bottom plate of a DHR-3 rheometer (TA Instruments, New Castle, DE) with a Peltier system controlling the temperature at 25 ± 0.1°C. A parallel plate fixture (20 mm diameter) was used with a measuring gap of 1000 μm. Oscillatory shear was continuously applied at 0.8 rad/s at a sampling interval of 30 s. Mixing and loading times were added to the start of the measurements to account for the short period of reaction before starting the measurement.

Preparation of collagen-glycosaminoglycan liquid suspensions
Nonmineralized (CG) and mineralized (CGCaP) collagen-glycosaminoglycan suspensions were prepared as previously

described (*5*). Briefly, CG suspensions consisted of 1% (w/v) type 1 collagen from bovine Achilles tendon (MilliporeSigma, Burlington, MA) and chondroitin-6-sulfate from shark cartilage (MilliporeSigma, Burlington, MA) at a ratio of 11.25:1, respectively, in 0.05 M acetic acid. CGCaP suspensions incorporated calcium salts [$Ca(OH)_2$ and $Ca(NO_3)_2 \cdot 4H_2O$] with the collagen and chondroitin-6-sulfate in a 0.1456 M phosphoric acid/0.037 M calcium hydroxide buffer solution to yield scaffolds with a calcium phosphate mineral content of 40 weight % (wt %) (*46*). Both suspensions were homogenized at 7000 rpm and 4°C to prevent collagen denaturation. Following homogenization, both suspensions were stored overnight at 4°C and degassed under vacuum before use.

Fabrication of biphasic and triphasic scaffolds

Biphasic scaffolds incorporating CG and CGCaP phases were fabricated as previously described (*5*). A mold comprising a PFTE body joined to a $^1/_{16}$-inch-thick copper base was used to induce directional solidification due to the mismatch in thermal conductivity during the freeze-drying process. First, CG suspension (550 μl) was pipetted into rectangular wells within the PFTE body (6 mm × 6 mm area; 30 mm deep). CGCaP suspension (550 μl) was then layered on top of the CG suspension, filling the well. The suspensions were then allowed to diffuse at room temperature for 20 min before freeze-drying. Triphasic scaffolds incorporating CG and CGCaP phases with an interfacial PEG-SH hydrogel seam were fabricated using a mold comprising three PFTE pieces, a $^1/_{16}$-inch-thick copper base plate, and a three-dimensional (3D)–printed acetyl-butyl-styrene (ABS) phase divider (fig. S2A). In the loading conformation (horizontal) with a phase divider inserted, the mold cavity was filled with both degassed collagen-glycosaminoglycan suspensions (500 μl each) and the polymerizing hydrogel solution (125 μl) using a micropipette (fig. S2B). After the phase divider was removed, the three phases were allowed to mix diffusively at their interface for 20 min at room temperature. The mold was then switched to its lyophilization (vertical) conformation, whereby the extensive mismatch in thermal conductivity between the PFTE body and copper base plate promotes unidirectional heat transfer through the copper base during lyophilization (fig. S2C). The suspension-loaded mold was placed into a freeze-dryer (VirTis, Gardiner, NY) held at 20°C for 5 min; then, the temperature was ramped down to −10°C at a rate of 1°C/min and held at −10°C for 2 hour to complete freezing. Immediately following freezing, the shelf temperature was ramped up to 0°C at a rate of 1°C/min, and scaffolds were dried via sublimation at 200 mtorr. For measuring freezing kinetics during lyophilization, ABS shelves of three different lengths (7.5, 15, and 22.5 mm) were 3D-printed. Immediately after loading the mold cavity, one shelf is inserted into the cavity, and all subsequent steps were carried out as before. Before lyophilization, a thermal probe is inserted into the shelf, with each shelf length corresponding to a scaffold phase based on its vertical location in the mold well (fig. S3A).

Triphasic scaffold imaging and measurement of interfacial width

Scaffolds were imaged using a FEI Quanta FEG 450 ESEM (FEI Company, Hillsboro, OR) at low vacuum. Interfacial hydrogel width was measured using the open-source image processing package Fiji (National Institutes of Health, Bethesda, MD) (*47*). Briefly, for each imaged triphasic scaffold, a reference scale was set (pixels/mm) on the basis of the ESEM image scale. Then, the longest and shortest

width of the hydrogel interface was measured, and the average of the two was reported as the hydrogel width for that scaffold.

Preparation of scaffolds for uniaxial tensile testing

Freeze-dried scaffolds were cut into a uniform length using a 3D-printed ABS cutting guide (21 mm total length: 12.5 mm from center to CG end and 8.5 mm from center to CGCaP end). Both scaffold ends were then embedded into hollow 3D-printed ABS end-blocks such that the scaffold interface was at the center of the exposed gauge length (15 mm), with equal lengths of CG and CGCaP exposed. End-blocks were used to protect scaffolds from being crushed by the pneumatic grips during mechanical testing. For the soft CG end, a two-component silicone rubber compound (RTV615; Momentive Specialty Chemicals Inc., Columbus, OH) at a ratio of 4:1 (A component:B component) was poured into a hollow end-block (5 mm deep) and allowed to partially cure at room temperature for 60 min before inserting the scaffold end. For the rigid CGCaP end, super glue (Loctite, Düsseldorf, Germany) was used to adhere the scaffold end into a shallow (1 mm deep) end-block. Mechanical testing was performed at least 24 hours after embedding to allow adhesive curing and ensure that scaffolds would not pull out of the end-blocks during mechanical testing. Test-ready embedded rectangular scaffolds were 5 mm thick and 5 mm wide with a 15-mm gauge length.

Uniaxial tensile testing

Uniaxial tensile testing was done using the Instron 5943 Mechanical Testing System with a 100-N electromechanical load cell (Instron, Norwood, MA). Scaffolds were held in place during testing by pneumatic grips at their end-blocks to prevent slippage. A preload was set to remove any slack from scaffolds, whereby scaffolds were strained at a rate of 0.1 mm/min until a load greater than 0.05 N was registered. Subsequently, the test would begin, and the scaffolds were strained at a rate of 1 mm/min until scaffold fracture. Elastic modulus was calculated as the slope of the linear elastic region of the stress-strain curve, and toughness was calculated as the area under the stress-strain curve (fig. S4B) (*28*, *48*, *49*).

Mapping local strain on scaffolds under tension using DIC

Scaffolds were prepared and embedded as previously described. Embedded scaffolds were then speckle-patterned with waterproof India ink (BLICK Art Materials, Galesburg, IL) using a gravity feed airbrush with a nozzle size of 0.3 mm (Got Hobby Inc., South El Monte, CA). Scaffolds underwent uniaxial tensile testing. During testing, images were captured using a Canon EOS 5DS R DLSR camera with a Canon Macro 100-mm lens at a rate of one image every 5 s using a time-lapse remote (Canon, Tokyo, Japan). Scaffold fracture mode was shown as the final image captured after fracture occurred. Sets of digital images taken during testing up to scaffold fracture were correlated using a version of the MATLAB file package "Digital Image Correlation and Tracking" (Copyright © 2010, C. Eberl, D. S. Gianola, and S. Bundschuh) modified by E. Jones (Improved Digital Image Correlation version 4—Copyright © 2013, 2014, 2015 by E. Jones) to calculate local strain across scaffolds. The DIC file package calculates local strain with respect to a region of interest (ROI). The ROI is specified in the first image of the set, and displacement is calculated from that first reference image for each subsequent image within the ROI up to scaffold fracture. The ROI was set as the entire exposed scaffold (Fig. 4A and fig. S5A) or

encompassing just the scaffold middle zone (Fig. 4B and fig. S5B). Strain in Fig. 4B and fig. S5B was calculated with respect to the total scaffold gauge length by equating the ratio of the length of the scaffold interface ROI to the total scaffold gauge length and the ratio of strain with respect to the scaffold interface ROI to strain with respect to the total scaffold gauge length. For each set of scaffold images, reduced images were correlated first to generate initial guesses for displacements in full images using individually optimized correlation settings (image reduction factor: 7; subset size: 21 to 61; threshold: 0.5; search zone: 3; grid step size: 5 to 10). Reduced correlations were iterated up to six times for image sets with high displacements. Subsequently, full images were correlated using the reduced image data (subset size: 21 to 61; threshold: 0.5; search zone: 2; grid step size: 5 to 10). Last, displacements were smoothed before calculating strains to reduce noise (Gaussian distribution of weights; kernel size: 11; number of smoothing passes: 3; maximum size of contiguous noncorrelated points to smooth over: 15), and local strains were calculated using a cubic (16-node) algorithm. Contour plots and line scans of strain could then be visualized. Line scan data were exported onto Microsoft Excel, and average strain was plotted as a function of position for each sample type.

Mechanical characterization of human cadaveric shoulder specimen

Human cadaveric shoulder specimens were acquired from an authorized tissue supplier (Science Care, Lombard, IL). Skin and all muscles were removed, except for the supraspinatus tendon and shoulder capsule. A custom in vitro apparatus was designed to simulate supraspinatus muscle loads during drill usage with the arm orientated at 90° of abduction. The apparatus applied a tensile force to the supraspinatus tendon via distraction of the supraspinatus muscle. The shoulder capsule and bone ends were fixed onto the apparatus using a two-part epoxy. The supraspinatus muscle was tensioned using a motor, and an S-load cell was placed in-line with the tension cable. Displacement and strain data were measured using a 3×4 grid drawn on the surface of the tendon-capsule complex along the supraspinatus tendon, resulting in nine strain regions per specimen (fig. S1A). A Panasonic Lumix FZ200 camera (Panasonic, Kadoma, Japan) was used to record the capsular surface grid at 100 FPS (frames per second). At 90° of abduction, the supraspinatus was tensioned, and the force and displacement data were recorded. Load cell force and image data from the camera were processed in MATLAB (MathWorks, Natick, MA) to analyze local strains and stiffness.

Statistical analysis

$n = 3$ samples for each hydrogel formulation were examined for rheological analysis of gelation, $n = 3$ samples for each scaffold condition were examined for measuring interfacial hydrogel width, and $n = 6$ samples for each scaffold condition were examined for uniaxial tensile testing. Statistical analysis was performed in RStudio (RStudio Inc., Boston, MA) using the programming language R (R Core Team, Vienna, Austria). Normality of the residuals for all samples was verified using a Shapiro-Wilk test, and homogeneity of variances was verified using Levene's test. Statistical analysis of data satisfying normality and homogeneity of variances was performed using one-way analysis of variance (ANOVA) followed by Tukey honest significant difference post hoc test. Statistical analysis of data not satisfying normality was performed using Kruskal-Wallis H test followed by Dunn's multiple comparison post hoc test. Statistical analysis of data not satisfying homogeneity of variance was performed using Welch's ANOVA followed by Games-Howell post hoc test. Statistical analysis of data not satisfying normality or homogeneity of variance was performed using a robust regression. Significance for all statistical analyses was set at $P < 0.05$.

REFERENCES AND NOTES

1. H. H. Lu, S. Thomopoulos, Functional attachment of soft tissues to bone: Development, healing, and tissue engineering. *Annu. Rev. Biomed. Eng.* **15**, 201–226 (2013).
2. A. C. Deymier, Y. An, J. J. Boyle, A. G. Schwartz, V. Birman, G. M. Genin, S. Thomopoulos, A. H. Barber, Micro-mechanical properties of the tendon-to-bone attachment. *Acta Biomater.* **56**, 25–35 (2017).
3. Y. X. Liu, S. Thomopoulos, V. Birman, J. S. Li, G. M. Genin, Bi-material attachment through a compliant interfacial system at the tendon-to-bone insertion site. *Mech. Mater.* **44**, 83–92 (2012).
4. G. M. Genin, A. Kent, V. Birman, B. Wopenka, J. D. Pasteris, P. J. Marquez, S. Thomopoulos, Functional grading of mineral and collagen in the attachment of tendon to bone. *Biophys. J.* **97**, 976–985 (2009).
5. S. R. Caliari, D. W. Weisgerber, W. K. Grier, Z. Mahmassani, M. D. Boppart, B. A. C. Harley, Collagen scaffolds incorporating coincident gradations of instructive structural and biochemical cues for osteotendinous junction engineering. *Adv. Healthc. Mater.* **4**, 831–837 (2015).
6. X. Ren, V. Tu, D. Bischoff, D. W. Weisgerber, M. S. Lewis, D. T. Yamaguchi, T. A. Miller, B. A. C. Harley, J. C. Lee, Nanoparticulate mineralized collagen scaffolds induce in vivo bone regeneration independent of progenitor cell loading or exogenous growth factor stimulation. *Biomaterials* **89**, 67–78 (2016).
7. J. C. Lee, C. T. Pereira, X. Ren, W. Huang, D. Bischoff, D. W. Weisgerber, D. T. Yamaguchi, B. A. Harley, T. A. Miller, Optimizing collagen scaffolds for bone engineering: Effects of cross-linking and mineral content on structural contraction and osteogenesis. *J. Craniofac. Surg.* **26**, 1992–1996 (2015).
8. X. Ren, D. Bischoff, D. W. Weisgerber, M. S. Lewis, V. Tu, D. T. Yamaguchi, T. A. Miller, B. A. C. Harley, J. C. Lee, Osteogenesis on nanoparticulate mineralized collagen scaffolds via autogenous activation of the canonical BMP receptor signaling pathway. *Biomaterials* **50**, 107–114 (2015).
9. D. W. Weisgerber, S. R. Caliari, B. A. Harley, Mineralized collagen scaffolds induce hMSC osteogenesis and matrix remodeling. *Biomater. Sci.* **3**, 533–542 (2015).
10. S. R. Caliari, B. A. C. Harley, Structural and biochemical modification of a collagen scaffold to selectively enhance MSC tenogenic, chondrogenic, and osteogenic differentiation. *Adv. Healthc. Mater.* **3**, 1086–1096 (2014).
11. S. R. Caliari, D. W. Weisgerber, M. A. Ramirez, D. O. Kelkhoff, B. A. C. Harley, The influence of collagen-glycosaminoglycan scaffold relative density and microstructural anisotropy on tenocyte bioactivity and transcriptomic stability. *J. Mech. Behav. Biomed. Mater.* **11**, 27–40 (2012).
12. S. R. Caliari, B. A. C. Harley, The effect of anisotropic collagen-GAG scaffolds and growth factor supplementation on tendon cell recruitment, alignment, and metabolic activity. *Biomaterials* **32**, 5330–5340 (2011).
13. W. K. Grier, E. M. Iyoha, B. A. C. Harley, The influence of pore size and stiffness on tenocyte bioactivity and transcriptomic stability in collagen-GAG scaffolds. *J. Mech. Behav. Biomed. Mater.* **65**, 295–305 (2017).
14. E. D. F. Ker, B. Chu, J. A. Phillippi, B. Gharaibeh, J. Huard, L. E. Weiss, P. G. Campbell, Engineering spatial control of multiple differentiation fates within a stem cell population. *Biomaterials* **32**, 3413–3422 (2011).
15. X. Li, J. Xie, J. Lipner, X. Yuan, S. Thomopoulos, Y. Xia, Nanofiber scaffolds with gradations in mineral content for mimicking the tendon-to-bone insertion site. *Nano Lett.* **9**, 2763–2768 (2009).
16. W. Liu, J. Lipner, J. Xie, C. N. Manning, S. Thomopoulos, Y. Xia, Nanofiber scaffolds with gradients in mineral content for spatial control of osteogenesis. *ACS Appl. Mater. Interfaces* **6**, 2842–2849 (2014).
17. D. Qu, C. Z. Mosher, M. K. Boushell, H. H. Lu, Engineering complex orthopaedic tissues via strategic biomimicry. *Ann. Biomed. Eng.* **43**, 697–717 (2015).
18. M. L. Killian, S. Thomopoulos, Scleraxis is required for the development of a functional tendon enthesis. *FASEB J.* **30**, 301–311 (2016).
19. A. G. Schwartz, F. Long, S. Thomopoulos, Enthesis fibrocartilage cells originate from a population of Hedgehog-responsive cells modulated by the loading environment. *Development* **142**, 196–206 (2015).

20. Y. Liu, A. G. Schwartz, V. Birman, S. Thomopoulos, G. M. Genin, Stress amplification during development of the tendon-to-bone attachment. *Biomech. Model. Mechanobiol.* **13**, 973–983 (2014).

21. Y. Li, C. Ortiz, M. C. Boyce, Stiffness and strength of suture joints in nature. *Phys. Rev. E Stat. Nonlin. Soft Matter Phys.* **84**, 062904 (2011).

22. K. Moriyama, K. Minamihata, R. Wakabayashi, M. Goto, N. Kamiya, Enzymatic preparation of a redox-responsive hydrogel for encapsulating and releasing living cells. *Chem. Commun.* **50**, 5895–5898 (2014).

23. C. W. Lee, S. A. Rogers, A sequence of physical processes quantified in LAOS by continuous local measures. *Korea Aust. Rheol. J.* **29**, 269–279 (2017).

24. R. Sun Han Chang, J. C.-W. Lee, S. Pedron, B. A. C. Harley, S. A. Rogers, Rheological analysis of the gelation kinetics of an enzyme cross-linked PEG hydrogel. *Biomacromolecules* **20**, 2198–2206 (2019).

25. F. J. O'Brien, B. A. Harley, I. V. Yannas, L. J. Gibson, The effect of pore size on cell adhesion in collagen-GAG scaffolds. *Biomaterials* **26**, 433–441 (2005).

26. F. J. O'Brien, B. A. Harley, I. V. Yannas, L. Gibson, Influence of freezing rate on pore structure in freeze-dried collagen-GAG scaffolds. *Biomaterials* **25**, 1077–1086 (2004).

27. N. McCormick, J. Lord, *Digital Image Correlation* (Materials Today, 2010), vol. 13, pp. 52–54.

28. L. C. Mozdzen, A. Vucetic, B. A. C. Harley, Modifying the strength and strain concentration profile within collagen scaffolds using customizable arrays of poly-lactic acid fibers. *J. Mech. Behav. Biomed. Mater.* **66**, 28–36 (2017).

29. E. Bayrak, P. Yilgor Huri, Engineering musculoskeletal tissue interfaces. *Front. Mater.* **5**, 24 (2018).

30. A. Seidi, M. Ramalingam, I. Elloumi-Hannachi, S. Ostrovidov, A. Khademhosseini, Gradient biomaterials for soft-to-hard interface tissue engineering. *Acta Biomater.* **7**, 1441–1451 (2011).

31. J. W. Hutchinson, Z. Suo, in *Advances in Applied Mechanics*, J. W. Hutchinson, T. Y. Wu, Eds. (Elsevier, 1991), vol. 29, pp. 63–191.

32. C. Z. Mosher, J. P. Spalazzi, H. H. Lu, Stratified scaffold design for engineering composite tissues. *Methods* **84**, 99–102 (2015).

33. A. Tampieri, M. Sandri, E. Landi, D. Pressato, S. Francioli, R. Quarto, I. Martin, Design of graded biomimetic osteochondral composite scaffolds. *Biomaterials* **29**, 3539–3546 (2008).

34. T. Shen, Y. Dai, X. Li, S. Xu, Z. Gou, C. Gao, Regeneration of the osteochondral defect by a wollastonite and macroporous fibrin biphasic scaffold. *ACS Biomater. Sci. Eng.* **4**, 1942–1953 (2017).

35. J. J. Li, K. Kim, S.-I. Roohani-Esfahani, J. Guo, D. L. Kaplan, H. Zreiqat, A biphasic scaffold based on silk and bioactive ceramic with stratified properties for osteochondral tissue regeneration. *J. Mater. Chem. B* **3**, 5361–5376 (2015).

36. G. Liu, Y. Li, L. Yang, Y. Wei, X. Wang, Z. Wang, L. Tao, Cytotoxicity study of polyethylene glycol derivatives. *RSC Adv.* **7**, 18252–18259 (2017).

37. C.-C. Lin, K. S. Anseth, PEG hydrogels for the controlled release of biomolecules in regenerative medicine. *Pharm. Res.* **26**, 631–643 (2009).

38. A. M. Kloxin, M. W. Tibbitt, A. M. Kasko, J. A. Fairbairn, K. S. Anseth, Tunable hydrogels for external manipulation of cellular microenvironments through controlled photodegradation. *Adv. Mater.* **22**, 61–66 (2010).

39. C. A. Deforest, E. A. Sims, K. S. Anseth, Peptide-functionalized click hydrogels with independently tunable mechanics and chemical functionality for 3D cell culture. *Chem. Mater.* **22**, 4783–4790 (2010).

40. S. Kobayashi, H. Uyama, S. Kimura, Enzymatic polymerization. *Chem. Rev.* **101**, 3793–3818 (2001).

41. W. J. McNamara, P. H. Lam, G. A. Murrell, The relationship between shoulder stiffness and rotator cuff healing: A study of 1,533 consecutive arthroscopic rotator cuff repairs. *J. Bone Joint Surg. Am.* **98**, 1879–1889 (2016).

42. Y. Liu, V. Birman, C. Chen, S. Thomopoulos, G. M. Genin, Mechanisms of bimaterial attachment at the interface of tendon to bone. *J.Eng. Mater. Technol.* **133**, 011006 (2011).

43. F. Saadat, A. C. Deymier, V. Birman, S. Thomopoulos, G. M. Genin, The concentration of stress at the rotator cuff tendon-to-bone attachment site is conserved across species. *J. Mech. Behav. Biomed. Mater.* **62**, 24–32 (2016).

44. A. K. Fung, J. J. Paredes, N. Andarawis-Puri, Novel image analysis methods for quantification of in situ 3-D tendon cell and matrix strain. *J. Biomech.* **67**, 184–189 (2018).

45. J. J. Paredes, N. Andarawis-Puri, Therapeutics for tendon regeneration: A multidisciplinary review of tendon research for improved healing. *Ann. N. Y. Acad. Sci.* **1383**, 125–138 (2016).

46. S. M. Best, R. E. Cameron, B. A. Harley, I. V. Yannas, L. J. Gibson, W. Bonfield, Design of a multiphase osteochondral scaffold. I. Control of chemical composition. *J. Biomed. Mater. Res. A* **92A**, 1057–1065 (2010).

47. J. Schindelin, I. Arganda-Carreras, E. Frise, V. Kaynig, M. Longair, T. Pietzsch, S. Preibisch, C. Rueden, S. Saalfeld, B. Schmid, J.-Y. Tinevez, D. J. White, V. Hartenstein, K. Eliceiri, P. Tomancak, A. Cardona, Fiji: An open-source platform for biological-image analysis. *Nat. Methods* **9**, 676–682 (2012).

48. N. Chandrashekar, J. Slauterbeck, J. Hashemi, Effects of cyclic loading on the tensile properties of human patellar tendon. *Knee* **19**, 65–68 (2012).

49. B. A. Harley, J. H. Leung, E. C. C. M. Silva, L. J. Gibson, Mechanical characterization of collagen–glycosaminoglycan scaffolds. *Acta Biomater.* **3**, 463–474 (2007).

50. L. J. Gibson, M. F. Ashby, B. A. Harley, *Cellular Materials in Nature and Medicine* (Cambridge Univ. Press, 2010).

51. A. Arampatzis, K. Karamanidis, K. Albracht, Adaptational responses of the human Achilles tendon by modulation of the applied cyclic strain magnitude. *J. Exp. Biol.* **210**, 2743–2753 (2007).

52. T. Stauber, U. Blache, J. G. Snedeker, Tendon tissue microdamage and the limits of intrinsic repair. *Matrix Biol.* **85–86**, 68–79 (2019).